JTTEE5 17:533–550
DOI: 10.1007/s11666-008-9209-x
1059-9630/$19.00 © ASM International



# Production of Nanoparticles in Thermal Plasmas: A Model Including Evaporation, Nucleation, Condensation, and Fractal Aggregation

*Norma Yadira Mendoza Gonzalez, Mbark El Morsli, and Pierre Proulx*

*(Submitted March 20, 2008; in revised form June 20, 2008)*

**In this work a coupled model for the production of nanoparticles in an inductively coupled plasma reactor is proposed. A Lagrangian approach is used to describe the evaporation of precursor particles and an Eulerian model accounting for particle nucleation, condensation, and fractal aggregation. The models of the precursor and nanoparticles are coupled with the magneto-hydrodynamic equations describing the plasma. The purpose of this study is to develop a model for the synthesis of particles in a thermal plasma reactor, which can be used to optimize industrial reactors. The growth of aggregates is considered by introducing a power law exponent $D_f$. Results are compared qualitatively and quantitatively with existing experimental data from plasma reactors at a relatively large laboratory scale. The results obtained from the model confirm the previously observed importance of the quench strategy in defining the morphology of the nanoparticles.**

**Keywords** CFD modeling, fractal particles, ICP plasmas, method of moments, nanoparticle synthesis

## 1. Introduction

Nanoparticles are a very important building block of the new nanotechnologies because of their often unusual optical, mechanical, catalytic, and electrical properties, and remarkably high specific surface areas (Ref 1). The processes used for generating nanoparticles play an important role on the product purity, size distribution, particle size, and particle morphology. Among the existing processes, high-frequency inductively coupled plasma (ICP) is an attractive method for synthesizing (Ref 2, 3). Good quality of particles including narrow size distribution, spherical shape, pure powder, and high production rates are the main features of the powders produced using this technology. Much improved control over temperature and gaseous mixtures over conventional flame technologies are also a very important feature of ICPs.

Detailed modeling of nanoparticle formation in plasma reactor has advanced in recent years to a degree that comparison with experimental results has become quantitative, as reported in the works of Ref 4-8. The experimental study of Goortani et al. (Ref 9) showed that the presence of agglomerates was largely controlled by the quench position and geometry of the reactor. In fact, in most cases of particle synthesis processes, there is the formation of agglomerates of individual spherical primary particles (Ref 10). The formation of particles consists of an initial phase of coalescent growth, where coagulation with small particles caused by high particle formation and rapid surface growth makes the particles to grow into near-spherical ''primary'' particles. The coalescent regime is followed by particle aggregation, when the particles take the form of fractal aggregates (Ref 11). The volume of the agglomerates can be related to their radius of gyration ($R_g$) by a power law, which can be used to explain the relationship between the mass and size. The exponent of this power law is called the mass fractal dimension (MFD), $D_f$ (Ref 12). The MFD $D_f$ determines the collision diameter of the agglomerates and subsequently their growth rate (Ref 13, 14). In addition, the dynamic behavior of these agglomerates is considerably different from their spherical counterparts. Several investigations of nonspherical particles in high-temperature synthesis of materials where agglomerates of individual spherical (primary) particles are formed have been reported (Ref 15-18).

Till date, different models have been used to explain the nature of the nanopowders produced in thermal plasma technology, where the nanoparticles are regarded as ideal spheres (Ref 6, 19, 20). In the present work, based on the ideas of Bilodeau (Ref 21), a Moment model is used to describe the initial evolution of the population of aerosol in the coalescent regime. To describe the aggregation regime, two other Moments equations are

**Norma Yadira Mendoza Gonzalez, Mbark El Morsli,** and **Pierre Proulx**, Laboratoire de Modélisation Mathématique des Procédés Chimiques OPPUS, Chemical Engineering Department, Université de Sherbrooke, Sherbrooke, QC, Canada J1K 2R1. Contact e-mail: norma.mendoza@usherbrooke.ca.

introduced, as suggested by Kazakov and Frenklach (Ref 11). The power law exponent $D_f$, which defines the type of irregular, fractal shape aggregates, is used.

To describe as completely as possible the process used to produce nanoparticles in actual industrial environment, the present model describes the evaporation of micron-sized particles used as precursor in the plasma (using a Particle-In-Cell Lagrangian modeling framework) and the formation of nanosized particles (using a moment transport Eulerian model). Both micron-sized and nanosized particle models are coupled with the fluid mechanical equations of continuity, momentum, and energy, and the vector potential formulation of the Maxwell's equations, that are used to describe the generation of the plasma. The mathematical model is solved using the commercial CFD software Fluent (release 6.2.16) software (Lebanon, NH), with the addition of numerous extensions to the commercial code through ''User-Defined Functions'' that had to be developed to take into account the specific physical and chemical aspects of the model. In the following sections, the model is described and applied to conditions similar to the measurements reported in Ref 9 and 22. The results showing the influence that the plasma and precursor loading parameters have on the formation of fractal particles is shown for the three different quench types used by Goortani co-workers (Ref 9, 22).

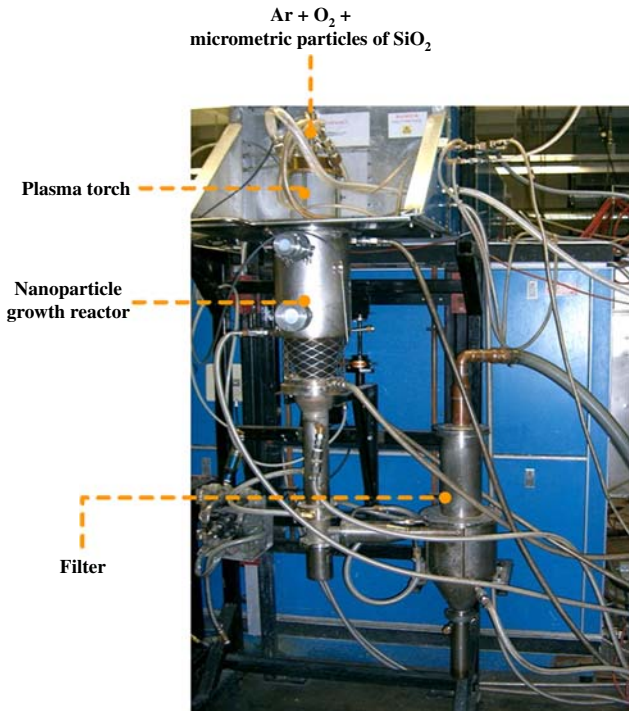


**Fig. 1** ICP nanopowder synthesis reactor at the CRTP of the Université de Sherbrooke

## 2. Model

The model developed in this study is applied to the reactor presented in Fig. 1. This ICP reactor is in use at the Plasma laboratory of the CREPE (Centre de Recherche en Énergie, Plasma et Électrochimie) at the Université de Sherbrooke. The induction tube is initially of 0.28 m in length and 0.025 m in radius. The radius is subsequently expanded to form a wider condensation tube ($r = 0.1$ m), often called the ''reactor'' zone. The induction torch has a rated operating power of 40 kW and is confined by water-cooled ceramic walls ($r = 0.025$ m). The plasma gases are argon and oxygen. Silica micron-sized particles are injected in the plasma zone where they evaporate and condense further downstream in the reactor. Pure oxygen is used as quench gas since it prevents silica from losing oxygen to SiO and also as a molecular gas, it represents a higher thermal load than other gases, e.g., argon (Ref 22). This produces a rapid temperature decrease that induces the vapor to condense and to produce fine aerosol particles. Silica-oxygen-argon is treated as an inert system but the model developed in this study can easily accommodate reacting systems.

### 2.1 Plasma Model

The inductively coupled thermal plasma torch has become a familiar tool in chemical analysis laboratories and is becoming an important tool in the production and treatment of advanced materials. In the last three decades, great progress has been made in mathematical modeling of the induction thermal plasma. Boulos (Ref 23) was the first to demonstrate, using Computational Fluid Dynamics (CFD) methods, the presence of the magnetic eddy in the heart of the discharge. The early model of Boulos used a one-dimensional formulation of the electromagnetic fields inside the coil, and a stream function, vorticity formulation of the Navier-Stokes equations with a general-purpose code. The original mathematical model of the ICP evolved significantly in the following decade. Two-dimensional electromagnetic models were introduced, as well as nonequilibrium models using two-temperature formulation, and plasma-particle interaction. More recently, another modification to the original model of Boulos (Ref 24) was introduced; the present work is based on this new approach. In the present model, no attempt to introduce swirling gas, as is used in most experimental setups, is made. This modification is made to simplify the model but should not, to the authors' knowledge, have a major impact on the results.

**2.1.1 Assumptions.** Figure 2 depicts the schematic of the ICP reactor used in this study. The geometry is considered as axisymmetric 2D with the axial coordinate $z$ and the radial coordinate $r$. The present system is assumed at steady state, in the turbulent regime, mainly in the reactor section where cooling and considerable recirculations occur. The main assumptions used are given in Table 1.

**2.1.2 Equations.** The governing equations of continuity, momentum, energy, and plasma species are presented below.

Continuity:

$$\frac{\partial(\rho u)}{\partial z}+\frac{1}{r}\frac{\partial(\rho r v)}{\partial r}=S_{\mathrm{m}} \qquad \text{(Eq 1)}$$

In Eq 1, $S_{\mathrm{m}}$ is the source term representing the mass added to the continuous phase from the dispersed phase (due to vaporization of the precursor micron-sized particles).

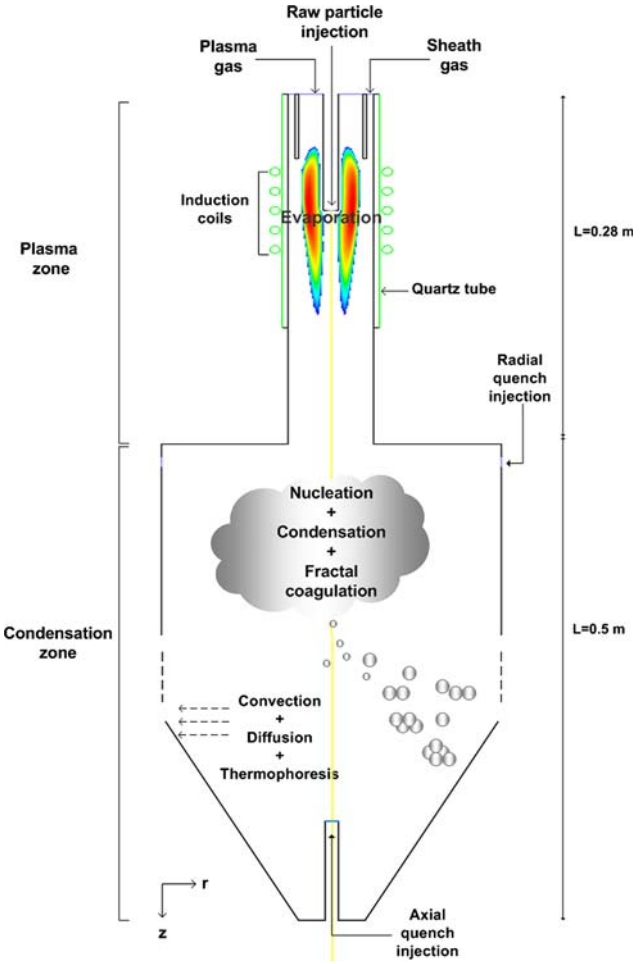


**Fig. 2** Schematic illustration of the ICP synthesis reactor

**Table 1 Fluid flow and temperature field assumptions**

- Steady state
- Axisymmetric flow at atmospheric pressure
- Turbulence modeled by the k-epsilon model modification proposed by Bolot et al. (Ref 25)
- The axial component of the coil current is neglected
- Radiative losses calculated from net emission coefficient, under local thermodynamic equilibrium (LTE) conditions
- Viscous dissipation and pressure work in the energy equation are neglected
- Negligible displacement current
- Nanoparticles do not affect the flow field or the turbulent quantities

Momentum:

$$\frac{\partial(\rho uu)}{\partial z}+\frac{1}{r}\frac{\partial(r\rho vu)}{\partial r}=\frac{\partial}{\partial z}\left(\mu_{\mathrm{eff}}\frac{\partial u}{\partial z}\right)+\frac{1}{r}\frac{\partial}{\partial r}\left(r\mu_{\mathrm{eff}}\frac{\partial u}{\partial r}\right)-\frac{\partial p}{\partial z}+\frac{\partial}{\partial z}\left(\mu_{\mathrm{eff}}\frac{\partial u}{\partial z}\right)+\frac{1}{r}\frac{\partial}{\partial r}\left(r\mu_{\mathrm{eff}}\frac{\partial v}{\partial z}\right)+F_z+F_{zb}+S_{p^z}^m \qquad \text{(Eq 2)}$$

$$\frac{\partial(\rho uv)}{\partial z}+\frac{1}{r}\frac{\partial(r\rho uu)}{\partial r}=\frac{\partial}{\partial z}\left(\mu_{\mathrm{eff}}\frac{\partial v}{\partial z}\right)+\frac{1}{r}\frac{\partial}{\partial r}\left(r\mu_{\mathrm{eff}}\frac{\partial v}{\partial r}\right)-\frac{\partial p}{\partial r}+\frac{\partial}{\partial z}\left(\mu_{\mathrm{eff}}\frac{\partial u}{\partial r}\right)+\frac{1}{r}\frac{\partial}{\partial r}\left(r\mu_{\mathrm{eff}}\frac{\partial v}{\partial r}\right)-2\mu_{\mathrm{eff}}\frac{v}{r^2}+F_r+F_{rb}+S_{p^r}^m \qquad \text{(Eq 3)}$$

Energy:

$$\frac{\partial}{\partial z}\left(\rho u\sum_i h_i\right)+\frac{1}{r}\frac{\partial}{\partial r}\left(r\rho v\sum_i h_i\right)=\frac{\partial}{\partial z}\left(\frac{\lambda_{\mathrm{eff}}}{Cp}\frac{\partial}{\partial z}\left(\sum_i h_i\right)\right)+\frac{1}{r}\frac{\partial}{\partial r}\left(r\frac{\lambda_{\mathrm{eff}}}{Cp}\frac{\partial}{\partial r}\left(\sum_i h_i\right)\right)+\sum_i\left[\frac{\partial}{\partial z}\left(\rho D_i h_i\frac{\partial Y_i}{\partial z}\right)+\frac{1}{r}\frac{\partial}{\partial r}\left(r\rho D_i h_i\frac{\partial Yi}{\partial r}\right)\right]+P^*+R+S_p^E \qquad \text{(Eq 4)}$$

where $u$ and $v$ are the axial and radial velocity components. ρ, μ, λ, and $Cp$ are the density, viscosity, thermal conductivity, and specific heat at constant pressure, respectively, $h$ is the enthalpy, $p$ is the pressure, and $P^*$ and $R$ are the Ohmic heating power and the volumetric radiation heat loss, respectively. The fluxes $J_j$ are the individual species mass fluxes. $F_{zb}$ is an artificial source term used to freeze the flow outside the plasma torch, a method not very elegant but efficient to fix flow conditions where it is not of interest, while solving some of the equations (electromagnetic) in the same region. $\mu_{\mathrm{eff}}=\mu_{\mathrm{l}}/\mu_{\mathrm{t}}$ is the effective viscosity, which is the combination of molecular and turbulent viscosities.

The Lorentz forces and Ohmic heating power are expressed as:

$$F_r=\frac{1}{2}\mu_0\sigma\mathrm{Re}\left(E_\theta H_z^*\right) \qquad \text{(Eq 5)}$$

$$F_z=-\frac{1}{2}\mu_0\sigma\mathrm{Re}\left(E_\theta H_r^*\right) \qquad \text{(Eq 6)}$$

$$P=\frac{1}{2}\mu_0\sigma\mathrm{Re}\left(E_\theta E_\theta^*\right) \qquad \text{(Eq 7)}$$

where $\mu_0$ is the magnetic permeability of free space, σ is the electric conductivity, and Re denotes the real part of a complex number. The superscript * denotes the conjugate.

The electromagnetic fields can be obtained by the following relations after solving the vector potential equations:

$$E_\theta=-\mathrm{i}\omega A_\theta \qquad \text{(Eq 8)}$$

$$\mu_0 H_z=\frac{1}{r}\frac{\partial(rA_\theta)}{\partial r} \qquad \text{(Eq 9)}$$

where ω is the angle frequency.

$$\mu_0 H_r = -\frac{\partial A_\theta}{\partial r} \quad \text{(Eq 10)}$$

$A_\theta$ is the tangential component of vector potential, which can be calculated as:

$$\nabla^2 A_\theta - \left(A_\theta / r^2\right) = -\mu_0 (J_{\text{coil}} + J_{\text{ind}}) \quad \text{(Eq 11)}$$

where

$$\nabla^2 = \frac{1}{r}\frac{\partial}{\partial r}\left(r\frac{\partial}{\partial r}\right) + \frac{\partial^2}{\partial z^2} \quad \text{(Eq 12)}$$

$J_{\text{coil}}$ is the current density induced by the oscillating voltage applied to the two ends of the coil and $J_{\text{ind}}$ is the current density developed in the plasma and the coil by the induced electric field.

### 2.2 Turbulence Model

Turbulent mixing may play an important role in particle processes in ICP torches but mostly in the reactor section (Ref 26). Recently, it was reported by Shigeta and Nishiyama (Ref 27) that turbulence must be accounted for even though the overall Reynolds number is relatively small. It is well known that plasma flame is often wavering and unstable accompanied with drastic heat/species transfer. The presence of strong turbulence in the particle formation zone, the reactor, is expected to affect the transport of the vapors and thus the trajectories of nanoparticles. Strong turbulent eddies may be present in the plasma reactor (mostly limited to the edges of the plasma) and their effect on the effective transport properties cannot be neglected.

In the present study, the k-epsilon model is selected. The choice of a more sophisticated model is difficult to justify since the amount of precise results of turbulent thermal plasmas that would be sufficient to distinguish the models are still today very scarce. The correction on the source term of the kinetic energy equation, proposed by Bolot et al. (Ref 25) is applied to this turbulent model; it was not originally adapted for high-temperature situations in Fluent 6.2.

The turbulent viscosity, $\mu_t$ is computed using $\kappa$ and $\epsilon$ as follows:

$$\mu_t = \rho C_\mu \frac{\kappa^2}{\epsilon} \quad \text{(Eq 13)}$$

where $\kappa$ is the turbulent kinetic energy, $\epsilon$ is the dissipation rate, and $C_\mu$ is a constant. The source term implemented for the correction in Fluent is:

$$S(\epsilon) = C_3 \frac{G^2}{\rho\kappa} \quad \text{(Eq 14)}$$

This sink term has no effect on most flows at low temperature, but it has a significant effect for turbulent plasma flows. It contributes to decrease the production of turbulent kinetic energy in the core of the jet, hence providing a longer core.

### 2.3 Particle Evaporation Model

In the synthesis of nanoparticles by thermal plasma, the precursor micron-sized particles are injected into the fireball to be evaporated. The particles are introduced in the model as a discrete second phase which consists of spherical particles dispersed in the continuous phase; the volume fraction occupied by the secondary phase is considered negligible. The trajectories of the discrete phase entities are computed using the equations describing the movement of a rigid particle in a fluid.

**2.3.1 Assumptions.** Table 2 summarizes the assumptions considered on the discrete phase model.

The discrete phase model considers the trajectory and heat-mass transfer coupling of particles with the continuum phase, this is the so-called PSI-Cell approach (Ref 28). Thus, the trajectory and heat-mass transfer calculations are based on the force balance on the particle and on the convective heat and mass transfer from the particle, using the local continuous phase conditions as the particle moves through the flow.

The thermophoresis effect is considered as an external force on the transport of particles. This effect is responsible for small particles in a temperature gradient driven from high to low temperature regions.

**2.3.2 Equations.** In the discrete phase model, the particle phase is regarded as a source of mass, momentum, and energy to the gaseous phase. The following equations are used to calculate the set of heat and mass transfer laws involved.

*Particle Motion*: Firstly, the trajectory of a discrete phase particle is calculated by integrating the force balance on the particle. This force balance equates the particle inertia with the forces acting on the particle and can be written as:

$$m_p \frac{du_p}{dt} = C_D \frac{1}{2}\rho\left(\frac{1}{4}\pi d_p^2\right)(u - u_p)|u - u_p| + F_{th} + m_p g + m_p F_b(t) \quad \text{(Eq 15)}$$

where $u$ is the fluid phase velocity, $m_p$ is the particle mass, $u_p$ is the particle velocity, $\mu$ is the molecular viscosity of the fluid, $\rho$ is the fluid density, $\rho_p$ is the density of the particle, $d_p$ is the particle diameter, $F_b(t)$ is the Brownian force per unit mass, and $F_{th}$ is the thermophoretic force.

The drag coefficient $C_D$ depends on the particle form and the relative Reynolds number Re, which is defined as:

$$\text{Re} \equiv \frac{\rho d_p |u_p - u|}{\mu} \quad \text{(Eq 16)}$$

**Table 2 Particle evaporation model assumptions**

- Particles are spheres and the fluid is an ideal gas
- Dispersion of particle due to turbulence by stochastic tracking model
- Dilute gas-particle system
- Continuous phase with a well-defined entrance and exit conditions
- Discrete phase solved in a Lagrangian frame of reference
- Coupling for momentum, heat, and mass between the plasma and the precursor microparticles
- Thermophoretic force and Brownian motion for submicron particles
- Gravity and turbulence have no influence

For a spherical particle, the drag coefficient $C_D$ is determined from:

$$C_D = \left(\frac{24}{\mathrm{Re}}\right) f(\mathrm{Re}) \quad \text{(Eq 17)}$$

where the $f(\mathrm{Re})$ functions are given according to the particle's boundary layer regime. As the Reynolds number increases, the Stokes and Oseen laws, and the empirical relations proposed by Boulos and Gauvin (Ref 29). The thermophoresis effect $F_{th}$ is included in the particle force balance following Ref 30. Besides, the Brownian motion $F_b(t)$ is considered since it becomes important for submicron particles. For the present study $F_b(t)$ is calculated as a Gaussian white noise random process (Ref 31) with spectral intensity $S_{nij}$ given by (Ref 32):

$$S_{n,ij} = S_0 \delta_{ij} \quad \text{(Eq 18)}$$

where $\delta_{ij}$ is the Kronecker delta function, and

$$S_0 = \frac{216 \nu k_B T}{\pi^2 \rho d_p^5 \left(\frac{\rho_p}{\rho}\right)^2 C_c} \quad \text{(Eq 19)}$$

where $T$ is the absolute temperature of the fluid, $\nu$ is the kinematic viscosity, $k_B$ is the Boltzmann constant, and $C_c$ is the Stokes-Cunningham slip correction which can be computed from:

$$C_c = 1 + \frac{2\lambda}{d_p}\left(1.257 + 0.4 e^{-\left(1.1 d_p / 2\lambda\right)}\right) \quad \text{(Eq 20)}$$

Amplitudes of the Brownian force components are of the form:

$$F_{b_i} = \zeta_i \sqrt{\frac{\pi S_o}{\Delta t}} \quad \text{(Eq 21)}$$

where $\zeta_i$ are zero-mean, unit-variance-independent Gaussian random numbers.

*Heat and Mass Transfer Calculations*: The particle temperature is determined through an energy balance as described in Ref 28. The total heat flux on a particle surface in the plasma $Q_T$ is given by:

$$Q_T = h_c \pi d_p^2 (T - T_p) - \pi d_p^2 \sigma_s \epsilon \left(T_p^4 - T_a^4\right) \quad \text{(Eq 22)}$$

where $d_p$, $h_c$, $T$, $T_p$, $\sigma_s$, $\epsilon$, and $T_a$, are the particle diameter (m), convective heat transfer coefficient (W/m$^2$·K), local temperature of the continuous phase (K), particle temperature, Stephan-Boltzmann constant, emissivity, and ambient temperature, respectively.

The heat transfer coefficient, $h_c$, is evaluated using the correlation of Ranz and Marshall (Ref 33, 34):

$$\mathrm{Nu} = \frac{h d_p}{k_\infty} = 2.0 + 0.6 \mathrm{Re}_d^{1/2} \mathrm{Pr}^{1/3} \quad \text{(Eq 23)}$$

where $k_\infty$ is the thermal conductivity of the continuous phase (W/m·K), $\mathrm{Re}_d$ is the Reynolds number based on the particle diameter and the relative velocity, and Pr is the Prandtl number of the continuous phase ($C_p \mu / k_\infty$).

The mass transfer during vaporization is predicted by a boiling rate. During droplet vaporization, the rate of vaporization is governed by gradient diffusion, with the flux of droplet vapor into the gas phase related to the gradient of the vapor concentration between the droplet surface and the bulk gas:

$$N_i = k_c \left(C_{i,s} - C_{i,\infty}\right) \quad \text{(Eq 24)}$$

where $N_i$ is the molar flux of vapor (kgmol/m$^2$s), $k_c$ is the mass transfer coefficient (m/s), $C_{i,s}$ is the vapor concentration at the droplet surface (kgmol/m$^3$), and $C_{i,\infty}$ represents the vapor concentration in the bulk gas (kgmol/m$^3$). The concentration of vapor at the droplet surface is evaluated by assuming that the partial pressure of vapor at the interface is equal to the saturated vapor pressure, $p_{sat}$, at the particle droplet temperature, $T_p$:

$$C_{i,s} = \frac{p_{sat}(T_p)}{R T_p} \quad \text{(Eq 25)}$$

where $R$ is the universal gas constant. The concentration of vapor in the bulk gas is known from solution of the transport equation for species $i$. The mass transfer coefficient in Eq 24 is calculated from a Nusselt correlation (Ref 33, 34):

$$\mathrm{Nu}_{AB} = \frac{k_c d_p}{D_{i,m}} = 2.0 + 0.6 \mathrm{Re}_d^{1/2} \mathrm{Sc}^{1/3} \quad \text{(Eq 26)}$$

where $D_{i,m}$ is the diffusion coefficient of vapor in the bulk (m$^2$/s); Sc is the Schmidt number, and $d_p$ is the particle diameter (m). The mass of the particle is reduced according to:

$$m_p(t + \Delta t) = m_p(t) - N_i A_p M_{w,i} \Delta t \quad \text{(Eq 27)}$$

where $M_{w,i}$ is the molecular weight of species $i$ (kg/kgmol); $m_p$ is the mass of the droplet (kg), and $A_p$ is the surface area of the particle (m$^2$).

### 2.4 Nanoparticle Model

The growth of particles is considered from nucleation to coalescent to aggregation (fractal) regimes, with simultaneously occurring nucleation and condensation of primary particles and coagulation of both primary and fractal particles. The different mechanisms of transport and growth are also considered.

**2.4.1 Equations.** *Nucleation*: Nucleation is caused by the fast cooling of the gas when it enters the condensation zone of the reactor. This phenomenon is strongly dependent of the vapor pressure of species in function of temperature. For the present model, the nucleation rate is formulated using the expression developed by Girshick (Ref 35). This expression is derived from a self-consistent equilibrium cluster distribution which results in a correction to the classical nucleation theory by a factor of $e^{\Theta}/S$, where $\Theta$ is a dimensionless surface energy defined by:

$$\Theta = \frac{\sigma s_1}{kT} \quad \text{(Eq 28)}$$

where $\sigma$ is the surface tension (under the capillarity approximation), $s_1$ is the surface area of a monomer (in this case a silica atom), $k$ is Boltzmann's constant, $T$ is absolute temperature, and $S$ is the vapor saturation ratio,

$S = n_1/n_s$; $n_1$ is the vapor concentration ($m^{-3}$) and $n_s$ is the vapor concentration at saturation ($m^{-3}$). The resulting expression for the nucleation rate is:

$$I = \frac{\beta_{11} n_s^2 S}{12}\sqrt{\frac{\Theta}{2\pi}}\left(\Theta - \frac{4\Theta^3}{27 ln^2 S}\right) \quad \text{(Eq 29)}$$

where $\beta_{11}$ is the Brownian coagulation coefficient between two monomers. The equation describing the evolution of the concentration $n_j$ of stable particle of size $j$ by nucleation is as follows:

$$\frac{dn_j}{dt} = I\delta_{(j-j^*)} \quad \text{(Eq 30)}$$

The Kronecker delta $\delta_{j-j^*}$ is defined as 1 for the critical size $j^*$ and zero otherwise.

*Condensation*: Surface condensation is the deposition of monomers on a stable particle of size equal to or larger than the critical size. Assuming that the size of a monomer is negligible compared to that of the particle, the growth law of a spherical particle in the free molecular regime is given by:

$$\frac{dv_j}{dt} = B_1 v_1 j^{2/3}(S-1) \quad \text{(Eq 31)}$$

with

$$B_1 = (36\pi)^{1/3} n_s v_1^{2/3} (kT/2\pi m_1)^{1/2} \quad \text{(Eq 32)}$$

where $v_j$ is the particle volume ($m^3$), $v_1$ and $m_1$ are the volume ($m^3$) and the mass (kg) of one monomer.

*Fractal Coagulation*: The dynamics of coagulation is fundamentally described by the Smoluchowski master equations, an enormous number of differential equations describing the population of different size particles. The evolution of the concentration ($n_j$) of stable particles of size $j$ is described by the following balance equation:

$$\frac{\partial n_j}{\partial t} = \frac{1}{2}\sum_{i+j=k} a\beta_{ij} n_i n_j - n_k \sum_{j=1}^{\infty} a\beta_{jk} n_j \quad \text{(Eq 33)}$$

where $a$ is the sticking coefficient which means the fraction of interparticle collisions that result in coalescence. $\beta_{i,j}$ is the coagulation coefficient classified on the basis of the Knudsen number: $Kn = 2\lambda/d$, where $\lambda$ is the gas mean free path and $d$ is the particle diameter (Ref 36). Because most of the particles are in the ultrafine range (i.e., $20 < Kn < 2000$ for the cases studied), and are smaller than the mean free path of flow gas, the collision frequency function due to Brownian motion is assumed in the free molecular regime. It is characterized by $Kn \gg 1$, in this situation, the following expression provided by Kazakov and Frenklach (Ref 11) expresses the collision frequency of particles:

$$\beta_{i,j} = 2.2\sqrt{\frac{6k_B T}{\rho}}\left(\frac{3m_{silica}}{4\pi\rho}\right)^{1/6}\sqrt{\frac{1}{m_i}+\frac{1}{m_j}}\left(m_i^{1/3}+m_j^{1/3}\right)^2 \quad \text{(Eq 34)}$$

where $k_B$ is the Boltzmann constant, $T$ is the temperature, $\rho$ is the density of particle material, $m$ is the particle mass (atomic mass units), $m_{silica}$ is the mass of a silica atom, and the multiplier 2.2 is the van der Waals enhancement factor.

*Thermophoresis*: The advection of particles is the result of the aerodynamic drag and the thermophoresis deviation. According to Ref 37, the thermophoretical velocity is independent of the particle size in the free molecular regime and the vectorial form is represented as follows:

$$\vec{u}_{th} = -\frac{0.55\mu}{\rho T}\vec{\nabla}T \quad \text{(Eq 35)}$$

*Brownian Diffusion*: The diffusion coefficient depends rather strongly on the particle size. Therefore, an average coefficient cannot be applied over the distribution of moments. In the case of small particles flowing in the high-temperature zones downstream of an ICP reactor, the Brownian motion becomes important. The evolution of the concentration $n_j$ of stable particle of size $j$ by Brownian diffusion is given by:

$$\frac{\partial n_j}{\partial t} = \vec{\nabla}\cdot\left(D_j\vec{\nabla}n_j\right) \quad \text{(Eq 36)}$$

in which $D_j$ is the diffusion coefficient of particles of size $d_j$ and the expression proposed by Phanse and Pratsinis (Ref 37) is used:

$$D_j = \frac{k_B T}{3\pi\mu d_j}\left(1 + \frac{3.314\lambda}{d_j}\right) \quad \text{(Eq 37)}$$

**2.4.2 Assumptions.** Several assumptions have to be made to make the model's equation tractable. Among these, the system must be a diluted system, where bulk vapor concentrations are smaller than $10^{-3}$ (kg/kg). Free molecular regime is considered because of the small size of the particles. Among the most important simplifications of the model is the assumption of a lognormal particle size distribution function. Using this hypothesis, it is possible to calculate the different moments of the particle size distribution in a closed form using only the first three moments of the distribution. The main outcome is the simplification of the equations to be solved, from a partial integro-differential equation to a set of three partial differential equations. Equally important, the agglomeration of particles is described by a power law. These assumptions are largely justified under the conditions used to generate nanoparticles in thermal plasmas (Ref 21). The assumptions are summarized in Table 3.

The contribution of the different mechanisms (nucleation, condensation, fractal coagulation, thermophoresis) are integrated in the general dynamic equation (GDE) for aerosol growth:

$$\vec{\nabla}\cdot(\vec{u}n_j) = -\vec{\nabla}\cdot(\vec{u}_{th}n_j) + \vec{\nabla}\cdot(D_j\vec{\nabla}n_j) + Ij^*\delta_{(j-j^*)} + G_{j-1}n_{j-1} - G_j n_j + \frac{1}{2}\sum_{i=j^*}^{j-1}\beta_{i,j-i}n_i n_{j-1} - n_j\sum_{i=j^*}^{\infty}\beta_{i,j}n_i \quad \text{(Eq 38)}$$

This equation must be solved to obtain the particle size distribution function (PSDF) of nanoparticles.

**Table 3 Silica vapor concentration and nanoparticle model assumptions**

- Particles are smaller that the mean free path of the gas: free molecular regime
- Coagulation of particles in the free molecular regime
- The condensible vapor is chemically inert
- The kinetic nucleation rate developed by Girshick and Chiu (Ref 35) is used
- The particle size distribution is approximated by a lognormal distribution
- The Kelvin effect is neglected
- Thermophoresis is accounted for as an external force in the transport of particles
- Particles follow the fluid flow (and thermophoretic deviation) and diffuse stochastically
- Because of Brownian diffusion
- Turbulence effect on particles is neglected
- Particle aggregation obeys a power law with constant fractal dimension $D_f$
- Five moments of the distribution are used to solve the fractal particle growth
- Three moments ($M_k$) solve for the primary particles and two moments ($P_r$)
- For the particle aggregation
- No surface growth terms are included in the aggregation regime

### 2.5 The Method of Moments

The population of different size particles is described by a finite but extremely large number of differential equations of the type of Eq 38 (Ref 36). Analytical solutions are possible for idealized, simple cases (as in Smoluchowski's solution) but the numerical integration of the equations as written up to this point is computationally untractable. The method of moments reformulates the problem into a small set of differential equations describing evolution of the moments of the PSDF. The method of moments is presented briefly in this section.

The first step in deriving the moment equations is to define the moments. The moment of the size distribution of order $k$ is defined as:

$$M_k = \frac{1}{\rho n_0}\sum_{j=j^*}^{\infty} j^k n_j \qquad \text{(Eq 39)}$$

where $n_0$ is a constant of normalization. In the present model, the moments of the size distribution are normalized with respect to the density ρ and the reference concentration of monomers $n_0$ at the entrance of the reactor. The number concentration, surface, and mass of particles in a given volume are obtained, respectively, from the moments M of order 0, 2/3, and 1. The moments of order 0, 1, and 2 are solved simultaneously with moments P described below.

For the moment of an arbitrary order $k$, the contribution of nucleation and surface condensation can be obtained directly by integrating Eq 30 and 31:

$$\frac{d(\rho M_k)}{dt}(\text{nucl},\text{cond}) = \frac{I}{n_0}(j^*)^k + \rho k B_1 (S-1) M_{k-1/3} \qquad \text{(Eq 40)}$$

After the initial period of nucleation followed by coalescent growth, particles begin to agglomerate. Agglomerates are assumed in the present work to take the form of chain-like structures composed of nearly spherical equal-sized primary particles and are described by the well-known fractal relationship (Ref 38):

$$n = k_f\left(\frac{2R_g}{d_p}\right)^{D_f} \qquad \text{(Eq 41)}$$

where $n$ is the number of primary particles in an aggregate, $d_p$ is the diameter of primary particle, $R_g$ is the radius of gyration of an aggregate, $D_f$ is the fractal dimension, and $k_f$ is the fractal prefactor. In the present model, particle agglomeration is considered at a fully developed regime of particle aggregation obeying Eq 41 with constants values of $D_f$ and $k_f$.

$$\beta_{i,j} = 2.2\sqrt{\frac{\pi k_B T}{2m_c}\left(\frac{1}{m_i}+\frac{1}{m_j}\right)}\left(d_{c,i}+d_{c,j}\right)^2 \qquad \text{(Eq 42)}$$

where $\beta_{i,j}$ is the aggregate collision frequency in the free molecular regime, $d_c$ is the collision diameter of a particle aggregate, and $d_{ci,j}$ represent the mobility diameters. Equation 42 is valid for $D_f \geq 2$ or for aggregates of similar sizes (Ref 39). The collision diameter of an aggregate, $d_c$, is proportional to the radius of gyration; the latter is given as:

$$R_g = \frac{1}{k_f^{1/D_f}}\left(\frac{3m_c}{4\pi\rho}\right)^{1/3} m^{1/3} n^{1/D_f - 1/3} \qquad \text{(Eq 43)}$$

which is obtained from Eq 41 expressing the primary particle diameter through the total aggregate mass $m$ and the number of primary particle in the aggregate $n$:

$$d_p = \left(\frac{6m_i m}{\pi\rho n}\right)^{1/3} \qquad \text{(Eq 44)}$$

The model for the aggregation is developed with the collision frequencies reflecting the fractal character of colliding particles (Ref 39):

$$\beta_{i,j}^{a} = 2.2\sqrt{\frac{\pi k_B T}{2m_{\text{silica}}}\left(\frac{1}{m_i}+\frac{1}{m_j}\right)}\left(d_{c,i}+d_{c,j}\right)^2 \qquad \text{(Eq 45)}$$

where $\beta_{i,j}$ is the aggregate collision frequencies in the free molecular regime and $d_c$ is the collision diameter of a particle aggregate.

Values of $D_f$ for silica particles around 2.2 are reported by the experimental works of Ref 40. As well, the experimental and numerical tests of Ref 41, related to the growth of silica particles influenced by high temperature, report values around 2.0. And additionally, values close to 2.4 are published from the numerical studies of Ref 42. In this work a constant value for $D_f$ = 2.0 is used. The influence of this parameter should be elucidated further but is not within the scope of the present study.

Assuming that in the limit of a single spherical particle $d_c$ becomes equal to the particle diameter:

$$d_c = d_p n^{1/D_f} = \left(\frac{6m_c}{\pi\rho}\right)^{1/3} m^{1/3} n^{1/D_f - 1/3} \qquad \text{(Eq 46)}$$

The following grid functions are obtained after substitution of Eq 46 into Eq 45 according to Kazakov and Frenklach (Ref 11) who determined the fractal coagulation term for the free-molecular coagulation of fractal particles,

$$\left\langle \varphi_{x,y}^{l} \right\rangle = 2.2\sqrt{\frac{6k_B T}{\rho}}\left(\frac{3m_{\text{silica}}}{4\pi\rho}\right)^{1/6}\left\langle f_{x,y}^{l} \right\rangle \quad \text{(Eq 47)}$$

where

$$\begin{aligned}\left\langle f_{x,y}^{l} \right\rangle &= \frac{1}{M_0^2}\sum_{i=1}^{\infty}\sum_{j=1}^{\infty}(m_i+m_j)^l\left(m_j^{1/3}n_j^{1/D_f-1/3}\right)^2 \\ &\quad \times m_i^{x-1/2}m_j^{y-1/2}N_iN_j \\ &= \sum_{k=0}^{l}\binom{l}{k}\left(\left\langle m^{x+k+1/6}n^{2/D_f-2/3}\right\rangle\mu_{y+l-k-1/2}\right. \\ &\quad + 2\left\langle m^{x+k-1/6}n^{1/D_f-1/3}\right\rangle\left\langle m^{y+l-k-1/6}n^{1/D_f-1/3}\right\rangle \\ &\quad \left. + \mu_{x+k-1/2}\left\langle m^{y+l-k+1/6}n^{2/D_f-2/3}\right\rangle\right) \quad \text{(Eq 48)}\end{aligned}$$

Terms $\langle m^r n^{r'}\rangle$ appearing in Eq 48 are approximated by the following relation (Ref 11):

$$\left\langle m^r n^{r'}\right\rangle \approx \langle m^r\rangle\left\langle n^{r'}\right\rangle = \mu_r\pi_{r'} \quad \text{(Eq 49)}$$

where $\langle m^r n^{r'}\rangle$ are binary moments of the two-dimensional particle size distribution, a function of both the aggregate mass $m$ and the aggregate number of primary particles $n$.

$$m^r = M_k = \frac{1}{\rho n_0}\sum_{j=j^*}^{\infty} j^k n_j \quad \text{(Eq 50)}$$

Moreover, the moments for the number of primary particles $\pi_r$ are determined by:

$$\pi_r = \frac{P_r}{P_0} \quad \text{(Eq 51)}$$

where

$$P_r = \sum_{1}^{\infty} n_i^r N_i \quad \text{(Eq 52)}$$

here, $N_i$ is the concentration of aggregate size class $i$, $n_i$ is the number of primary particles in $i$th aggregate, and $P_0$ is equivalent to $M_0$, the total aggregate number density. The physical meaning of the $\pi_r$ moments is as follows: $\pi_0 \equiv 1$, $\pi_1$ is the average number of primary particles in aggregates. Moments $P_r$, describing the fractal geometry of aggregates, are solved simultaneously with the moments $M_k$, describing the coalescent regime.

For moments $P_r$, the aggregate coagulation in the free molecular regime is calculated with:

$$H_r = \frac{1}{2}\langle\psi_r\rangle \quad \text{(Eq 53)}$$

with $\langle\psi_r\rangle$ evaluated by interpolation between grid functions:

$$\left\langle \psi_r^l \right\rangle = 2.2\sqrt{\frac{6k_B T}{\rho}}\left(\frac{3m_{\text{silica}}}{4\pi\rho}\right)^{1/6}\left\langle h_r^l \right\rangle \quad \text{(Eq 54)}$$

where

$$\begin{aligned}\left\langle h_r^l \right\rangle &= \sum_{k=0}^{l}\binom{r}{k}\sum_{q=0}^{r-1}\binom{r}{q}\left(\left\langle m^{k+1/6}n^{q+2/D_f-2/3}\right\rangle\left\langle m^{l-k-1/2}n^{r-q}\right\rangle\right. \\ &\quad + 2\left\langle m^{k-1/6}n^{q+1/D_f-1/3}\right\rangle\cdot\left\langle m^{l-k-1/6}n^{r-q+1/D_f-1/3}\right\rangle \\ &\quad \left.\left\langle + m^{k-1/2}n^q\left\langle m^{l-k+1/6}n^{r-q+2/D_f-2/3}\right\rangle\right\rangle\right) \quad \text{(Eq 55)}\end{aligned}$$

The binary moments appearing in these equations are obtained via approximation 50 and the fractional order moments by interpolation between the whole order moments using the approach described by Frenklach and Harris (Ref 43).

The dynamics of particle coagulation is described for the following set of equations:

$$\frac{d(\rho M_0)}{dt}(\text{coag}) = -\frac{\rho^2 n_0}{2}\Phi_{0,0}M_0^2 \quad \text{(Eq 56)}$$

$$\frac{d(\rho M_1)}{dt}(\text{coag}) = 0 \quad \text{(Eq 57)}$$

$$\frac{d(\rho M_2)}{dt}(\text{coag}) = \rho^2 n_0\Phi_{0,0}M_1^2 \quad \text{(Eq 58)}$$

$$\frac{d(\rho P_1)}{dt}(\text{frac}) = 0 \quad \text{(Eq 59)}$$

$$\frac{d(\rho P_2)}{dt}(\text{frac}) = H_r \quad \text{(Eq 60)}$$

The contribution of the different mechanisms (nucleation, condensation, coagulation, thermophoresis) described above are transformed in terms of moments of the distribution; therefore, transport equations for the moments of the PSDF are obtained:

$$\begin{aligned}&\frac{\partial(\rho M_k)}{\partial t} + \vec{\nabla}\cdot(\rho\vec{u}_{\text{th}}M_k) = -\vec{\nabla}\cdot(\rho\vec{u}_{\text{th}}M_k) + \vec{\nabla}\cdot(\rho\bar{D}\vec{\nabla}M_k) \\ &+ \frac{I}{n_0}(j^*)^k + kB_{1\rho}(S-1)M_{k-1/3} + \frac{\rho^2 n_0}{4}[k^2+k-2]\Phi_{0,0}M_{k/2}^2 \quad \text{(Eq 61)}\end{aligned}$$

By a mass balance over the aerosol and the vapor, the conservation of the monomer in vapor phase is as follows:

$$\begin{aligned}&\frac{\partial(\rho\omega_1)}{\partial t} + \vec{\nabla}\cdot(\rho\vec{u}_{\text{th}}\omega_1) = \vec{\nabla}\cdot(\rho D_1\vec{\nabla}\omega_1) \\ &\qquad - Ij^*m_1 - B_1\rho n_0 m_1(S-1)M_{k-1/3} \quad \text{(Eq 62)}\end{aligned}$$

## 3. Solution Method

The geometry of the reactor is axisymmetric; therefore, the ICP reactor is represented by a 2D computational

domain. Silica-oxygen-argon is assumed to be a chemically inert system. The final scalar equations set is summarized in Table 4. The computational simulation is performed for a grid system (see Fig. 3) of 80,000 cells; numerical accuracy tests were performed to insure results' grid independence.

### 3.1 Transport Properties and Boundary Conditions

To calculate the mixture properties, mass-weighted mixing law is used to calculate density, thermal conductivity, and viscosity. The mass diffusion coefficient is calculated from kinetic theory and specific heat is calculated with a mixing law.

The precursor particles are assumed to follow the Rosin-Ramler distribution function. This is based on the assumption that an exponential relationship exists between the raw particle diameter, $d$, and the mass fraction of raw particles with diameter greater than $d$, $Y_d$:

$$Y_d = e^{-(d/\bar{d})^n} \quad \text{(Eq 63)}$$

where $\bar{d}$ is the size constant and $n$ is the size distribution parameter. The injected $SiO_2$ raw particles have a logarithmic distribution with diameters summarized in Table 5. Equally important, conditions like, position, velocity, size, and temperature of individual raw particles must to be defined to calculate the discrete phase (see Table 5).

**Table 4 Source terms for the moments of the PSDF**

| Equation | $S_c$ | $S_p$ |
|---|---|---|
| $M_0$ | $-\vec{\nabla}(\rho\vec{u}_{th}M_0) + \frac{I}{n_0} + \frac{\rho^2 n_0}{2}\Phi_{0,0}M_0^2$ | $-\rho^2 n_0 \Phi_{0,0} M_0$ |
| $M_1$ | $-\vec{\nabla}(\rho\vec{u}_{th}M_1) - \frac{I}{n_0}j^* + B_{1\rho}(S-1)M_{2/3}$ | 0 |
| $M_2$ | $-\vec{\nabla}(\rho\vec{u}_{th}M_2) + \frac{I}{n_0}(j^*)^2 + \rho^2 n_0 \Phi_{0,0} M_1^2 + 2B_{1\rho}(S-1)M_{5/3}$ | 0 |
| $P_1$ | $-\vec{\nabla}(\rho\vec{u}_{th}P_1) + \frac{I}{n_0}$ | 0 |
| $P_2$ | $-\vec{\nabla}(\rho\vec{u}_{th}P_2) + \frac{I}{n_0} + H_r$ | 0 |

The density, the viscosity, the thermal conductivity, the specific heat at constant pressure, and the radiation losses for plasma gas are obtained from Ref 44. Physical properties for silica are summarized in Table 6 according to Ref 20.

The boundary conditions are obtained from the following operating conditions: pure argon is injected at the entrance of the reactor in a stream called the plasma gas (q2) and the precursor particles are injected through the central carrier flow (q1). A mixture of oxygen and argon is injected through the so-called sheath gas flow (q3). The other flow rates q4 and q5 are quench flows used for radial and axial quench, respectively. The quench gas is oxygen. The walls of the reactor are set to 300 K. At the end of the nanoparticle reactor, radial gradients are assumed to be zero for all variables. The centerline condition is naturally zero gradients and zero radial velocity.

### 3.2 Numerical Procedure

The mathematical model including the governing equations for momentum, energy, mass concentration, and electromagnetic fields, along with the boundary conditions, is solved using Fluent. Since Fluent is a general-purpose code, many of the equations of the model have to be supplied through so-called user-defined functions. In these, the specific physical aspects of the model can be included.

**Table 5 Injection properties for the silica raw particles**

| | |
|---|---|
| Inlet velocity, m/s | 25 |
| Temperature, K | 300 |
| Mass flow rate, gpm | 1.5 |
| Maximum diameter, m | $5 \times 10^{-6}$ |
| Mean diameter, m | $2 \times 10^{-8}$ |
| Minimum diameter, m | $2.6 \times 10^{-6}$ |

**Table 6 Physical properties for silica**

| | |
|---|---|
| Viscosity (Pa·s) | $Ae^{U/RT}$ |
| Specific heat capacity | 1427.51 |

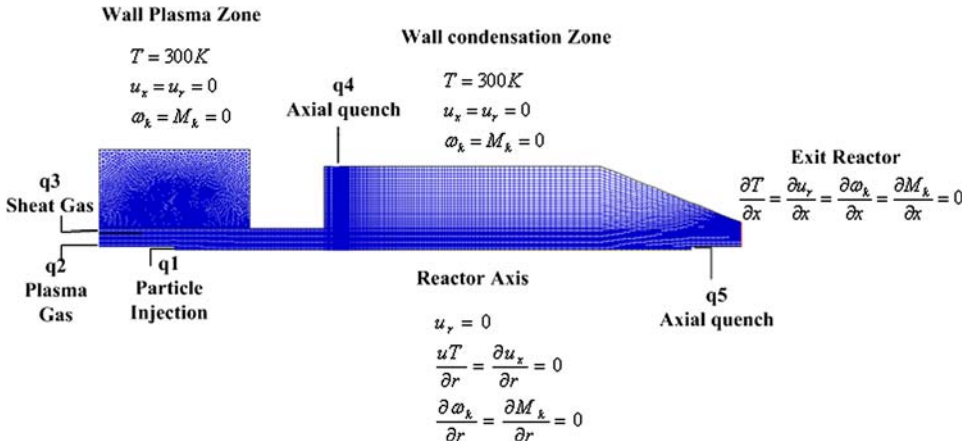


**Fig. 3** Grid reactor

To obtain satisfactory convergence and stability, since there is a very strong coupling between all the physical phenomena involved in the model (electromagnetic, heat, momentum and heat transfer, nucleation), the following model solution procedure was used:

(1) Solve the continuous phase: electromagnetic, fluid flow, heat, and mass transfer equations.
(2) Create the discrete-phase injections.
(3) Solve the plasma-particle coupled flow.
(4) Track the discrete-phase injections.
(5) Solve the 5 moments with species equation without any nanoparticle source terms.
(6) Include the source terms for nucleation.
(7) Include the condensation term.
(8) Include the fractal coagulation term.

For the nanoparticle model solution, starting at step 5, the moments are activated only once the fluid flow is converged. Convergence is assumed when the relative residues for the vector potential equations, the continuity, velocities, energy and moments are, respectively, under $10^{-8}$, $10^{-4}$, $10^{-5}$, $10^{-6}$, and $10^{-7}$. Typical solution time is of the order of 5 h in a single Pentium IV.

## 4. Results and Discussion

The model is applied to the ICP reactor presented in Fig. 1. Three different designs are studied based on the experimental studies of Goortani and coworkers (Ref 9, 22). The first reactor (''No quench'') does not have any quench, only cold walls in the condensation zone. In the second reactor, quench gas is injected radially (since the geometry is axisymmetrical, it corresponds to an annular quench) from the top of the reactor, zone (q4), (''Radial quench''). The third design uses an axial counter-current quench from zone (q5), (''Axial quench'').

### 4.1 Plasma Generation and Particle Evaporation

**4.1.1 Temperature and Flow Fields.** The Fig. 4 presents the temperature field in the three different reactor geometries. In the plasma zone, the highest values of those temperatures are of the order of 10,000 K as expected. Downstream of the plasma zone, where nanoparticles will form by nucleation, lower temperature values are due to cold walls and/or because of the application of quench. This temperature drop combined with the strong convection rapidly leads to highly supersaturated vapors which induces the nucleation burst. The temperature field and the silica

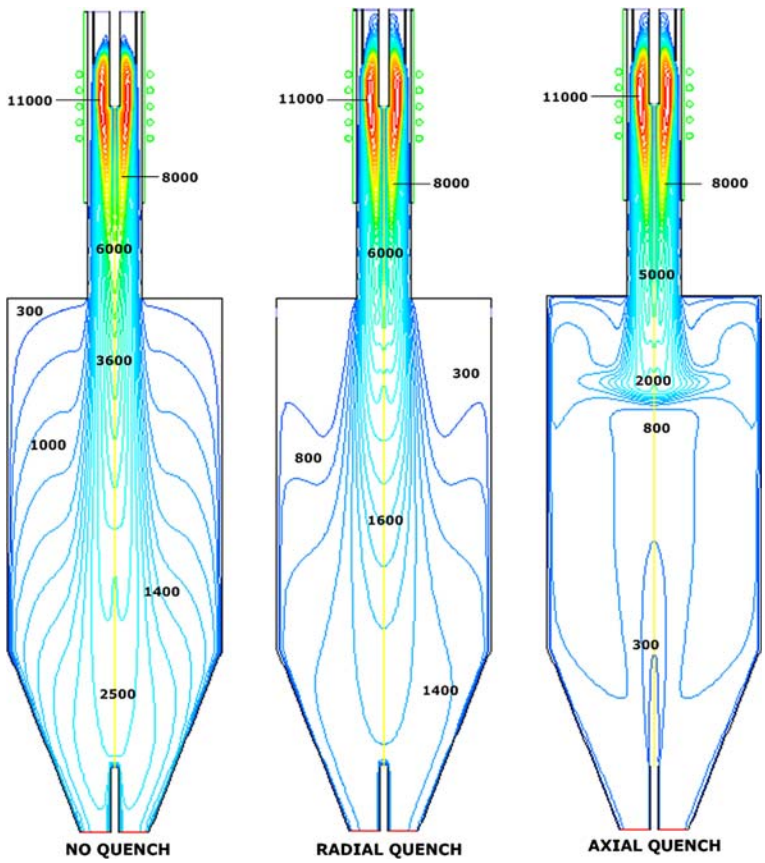


**Fig. 4** Temperature contours (K)

vapor concentration indicate where the particles are formed or grow by nucleation and/or condensation. The temperature fields in the ''reactor,'' or condensation zone, will largely determine the vapor pressure, the condensation rate, the coagulation rate, and the thermophoretic term.

In the cases with radial or axial quench, the hot gas is mixed with the quenching stream and the temperature at the recirculation zone decreases rapidly. After the recirculation zone, the hot gas in the center of the reactor is strongly mixed by turbulence with the cold gas from the recirculation. The exit temperature of the reactor is almost uniform at 1500 K for the ''No quench'' and the ''Radial quench'' cases. On the other hand, the ''Axial quench'' case shows a lower temperature value at the exit, around 500 K, it seems to be a more efficient quench. At this temperature the vapor pressure of the silica is very low leaving most of the material condensed.

The streamlines are shown in Fig. 5. An important recirculation is observed above the coil region. The central injection tube splits this recirculation, so that the powders of the precursors can be injected directly into the high-temperature region. The turbulence is shown through the turbulence viscosity ratio contours in Fig. 6. The ratio of the turbulent viscosity to the molecular viscosity indicates well the high level of mixing attained in particular in the reactor with axial quench.

**4.1.2 Mass Fraction Fields.** After injecting the precursor particles in the plasma torch, they are carried by the argon flow to the plasma zone where they rapidly evaporate. Figure 7 shows the mass fraction for the three cases. It is observed that for the three cases, evaporation is practically the same as indicated by the mass fraction contours but the quench method has little influence upstream. However, there are important differences in the condensation zone of the reactor due to the quench method applied.

The high vapor concentration created in the plasma zone is transported further into the condensation zone of the reactor. The concentration of silica vapor is depleted when the nucleation burst begins. This concentration will also decrease due to the condensation of species vapor on existing particles at the wall and by dilution in the case of quench injection. Once again the ''Axial quench'' method seems to be more efficient in terms of mass fraction decrease.

Figure 8-10 shows the particle (precursor) temperature as a function of the distance traveled in the axial direction of the reactor for the three studied cases: No quench, Radial quench, and Axial quench, respectively. From these figures, two lines are observed representing a first group of particles evaporated immediately entering the plasma zone and a second group further when they reach

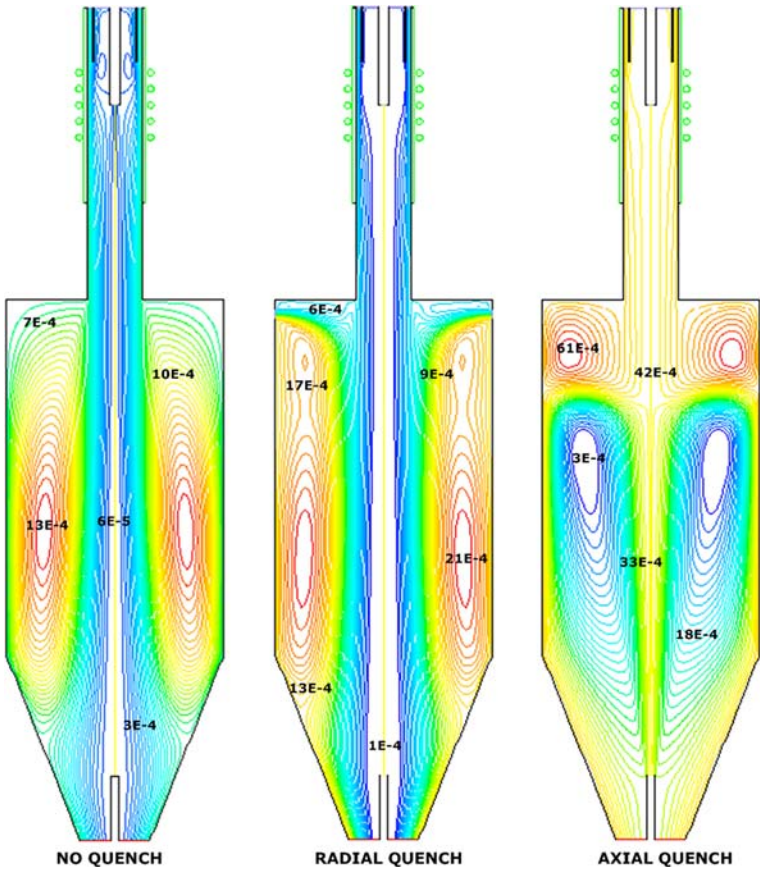


**Fig. 5** Stream function contours (kg/s)

their boiling point (2800 K). There is a similitude of the location for the first evaporated group but the second one behaves differently. Figure 8 shows that the second evaporation takes place around 9 cm after injection, while in Fig. 9 and 10, the second evaporation takes place at the end of the torch around 18 cm after injection. This shows that the quench has an upstream effect in the present configuration; it affects also the evaporation zone. It is also noted that the injection rate of particles has an important influence on the temperature fields of the plasma zone. A high particle rate injection produces a temperature decrease as observed in Fig. 11. This effect was first predicted by mathematical modeling by Proulx et al. (Ref 45) who studied the plasma-particle interaction under dense loading conditions in induction plasmas.

### 4.2 Effect of Nanoparticle Growth

In the first stage of particle growth, the nucleation burst is observed clearly through the numerical mean diameter presented in Fig. 12. Nucleation is the formation of new particles and therefore increases the density of particles. Following that, the mean numerical diameter of primary particles ($d_{num}$) is depicted to observe the formation and growth mechanism effects. The mean numerical diameter is a physical property of the PSDF in terms of the moments, $d_{num} = d_1(M_{1/3}/M_0)$ (Ref 21). Where $d_1$ is the atomic size of a silica particle, $M_{1/3}$ and $M_0$ are calculated moments of the PSDF.

After nucleation, the primary particles continue to grow by condensation and coagulation processes. Figure 13 shows the particle size attained after nucleation and condensation growth. In the case without quench, large particles are formed near the walls and close to the exit with sizes over the 100 nm, contrary, cases with quench injection show smaller sizes. This fact confirms that using quench strongly promotes the nanoparticle formation with a controlled size range. The advantage of quench is also observed by Shigeta and Watanabe (Ref 46) where the effect of radial and counterflow cooling gas injection is studied.

The final size of primary particles at the onset of fractal coagulation is depicted on Fig. 14. The coagulation produces an increase in the final particle size; nevertheless, the condensation mechanism seems to have a dominant contribution in the growth of nanoparticles subsequent to nucleation, as already observed by Bilodeau and Proulx (Ref 47). This fact can be dependent also on the kinds of materials as reported by Shigeta and Watanabe (Ref 48), who showed that for the case of nonmetals such as boron and silicon, the dominant growth process is the heterogeneous condensation.

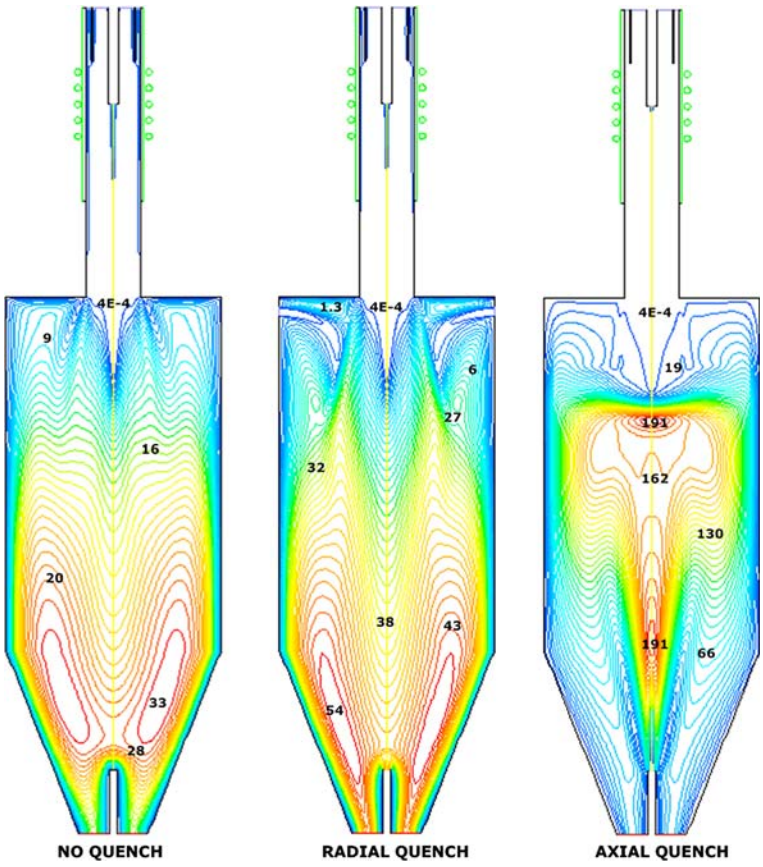


**Fig. 6** Turbulent viscosity ratio

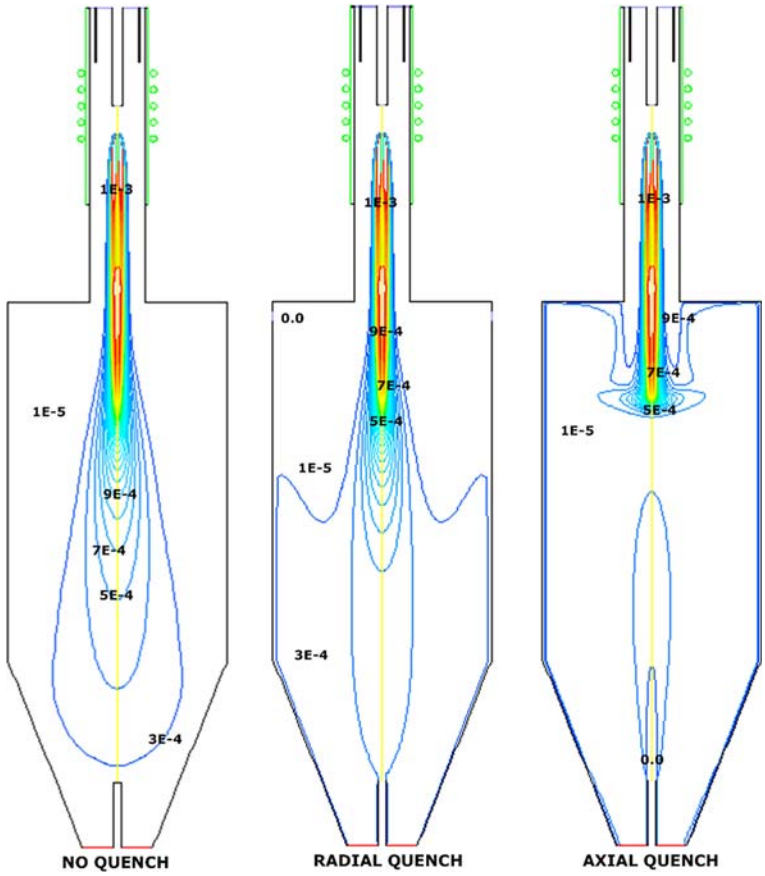


**Fig. 7** Mass fraction contours

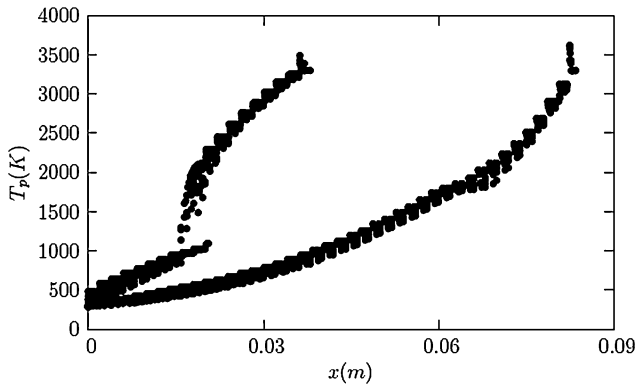


**Fig. 8** Temperature history of silica particles injected into argon/oxygen plasma (No quench)

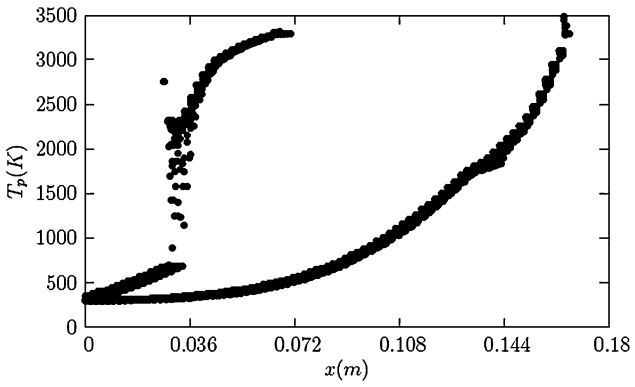


**Fig. 9** Temperature history of silica particles injected into argon/oxygen plasma (Radial quench)

### 4.3 Effect of Nanoparticle Aggregation

The initial number of primary particles per aggregate is shown in Fig. 15 for the three cases studied. After the aggregation is switched on in the model, the average primary particle diameter starts to increase, due to surface growth, and remains nearly constant once the surface growth rate decreases. If we relate Fig. 14 and 15, we can see that the average number of primary particles per aggregate is larger where primary diameters are smaller.

The quench has a direct influence on the volume distribution and structure of fractal aggregates. This is because recirculations produce more collisions among primary particles and hence bigger agglomerates are formed. This fact is observed in the radial and axial quench cases. Contrary, the case of the ''No quench''

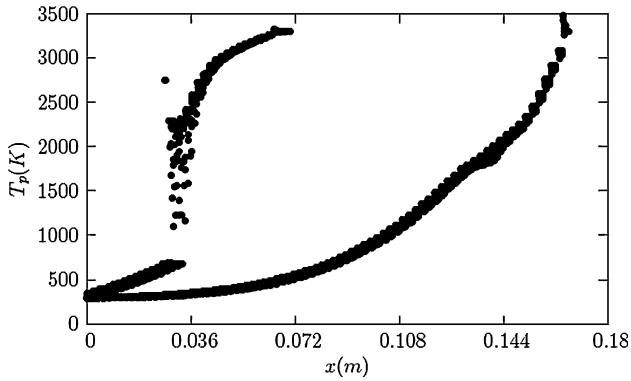


**Fig. 10** Temperature history of silica particles injected into argon/oxygen plasma (Axial quench)

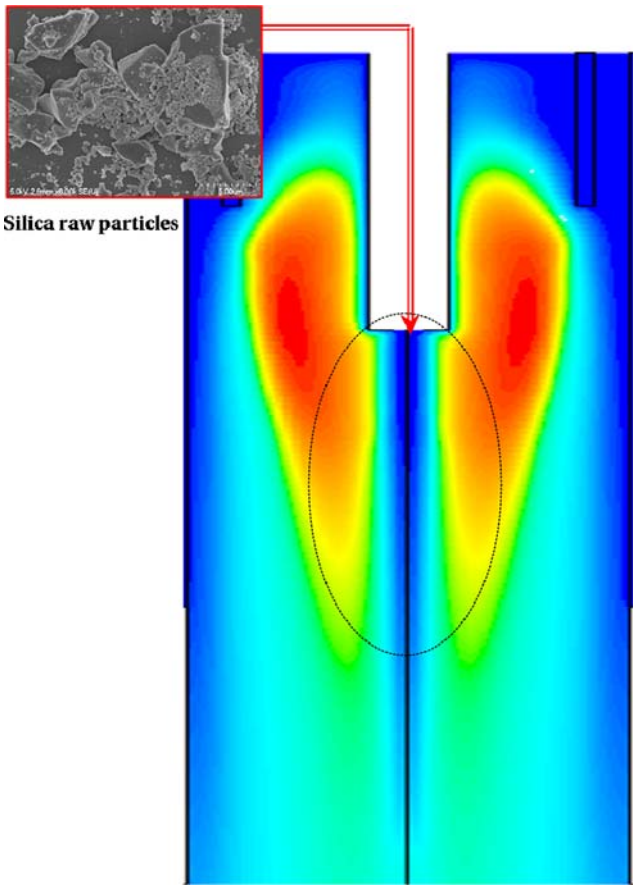


**Fig. 11** Influence of particle injection rate on temperature fields

where collisions are less important creates a smaller number of aggregates.

### 4.4 A Reactor Design for Spherical Nonaggregated Nanoparticles

The three different quench designs analyzed have shown a high level of aggregation. To obtain spherical nonagglomerated particles, a reactor was proposed by Goortani et al. (Ref 9). This "Alumina wall reactor," consists simply of a 60 cm alumina tube, 10 cm internal diameter, and it is installed within a stainless steel, water-cooled support at the exhaust of the plasma torch. The 3D geometry used for this study represents only the condensation zone, not the plasma generation zone.

Figure 16 presents the temperature contours of the "Alumina wall reactor." It is observed that the contours are smooth so that can favor a more complete evaporation of particles and the presence of small temperature gradients. Figure 17 shows the primary particle sizes with diameters from 30 to 58 nm. Figure 18 depicts the number of primary particles per aggregate showing a maximum value of 4 particles per aggregate. This is the lowest value in the reactors studied here confirming the efficiency of this design to produce nonaggregate particles. This result is in good agreement with the qualitative experimental findings of Ref 9. Furthermore, half of the volume of the reactor generates purely spherical particles. In addition, it is observed that the particle aggregation occurs near the quench injection point and reaches a maximum value close to the reactor exit.

Table 7 summarizes the experimental data and the numerical results obtained from the present model. The experimental particle size corresponds to the equivalent diameter $D(3,2)$ based on the specific surface area of the powder. Experimental particle size is measured as collected from the filter, while numerical results corresponds to the mixing cup diameter $D_{\text{cup}}$ obtained at the exit of the reactor. The mixing cup diameter is calculated using Eq 64.

$$D_{\text{cup}} = \frac{\int d_{\text{num}} \rho \vec{v} \cdot \overrightarrow{dA}}{\int \rho \vec{v} \cdot \overrightarrow{dA}} \qquad \text{(Eq 64)}$$

It is seen that the agreement between primary particle sizes predicted by the model and the experimental results is quite good. The fractal particles results are also in good qualitative agreement, even though from the experimental study only a qualitative description of aggregation is available. It is important to note that at the present stage of investigations, the comparison of experimental and simulation data is still limited. Further investigations are required to better interpret the similarities and differences noted between the model and measured data.

## 5. Conclusions

A two-dimensional axisymmetric turbulent model of an ICP reactor used to produce nanopowders from solid precursors is developed. It is applied to four different quench methods corresponding to four reactors previously studied. The evolution of the particle size distribution is calculated using the method of moments (MOM) and assuming a lognormal particle size distribution. Five moments are considered to calculate the formation and growth of fractal particles.

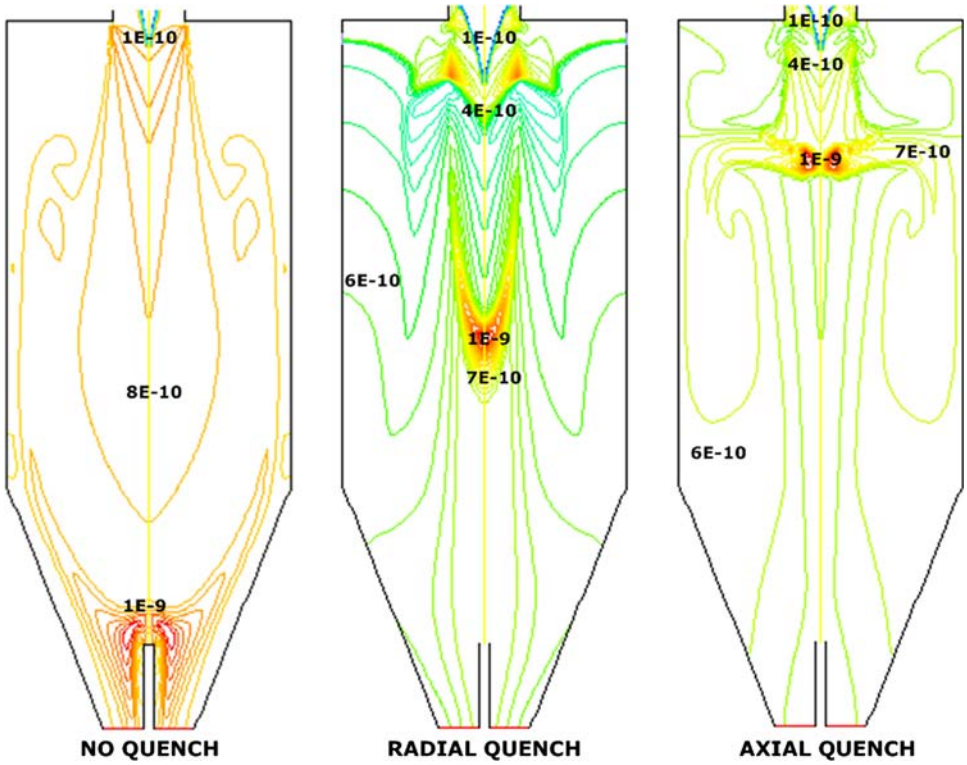


**Fig. 12** Numerical diameter (m) after nucleation

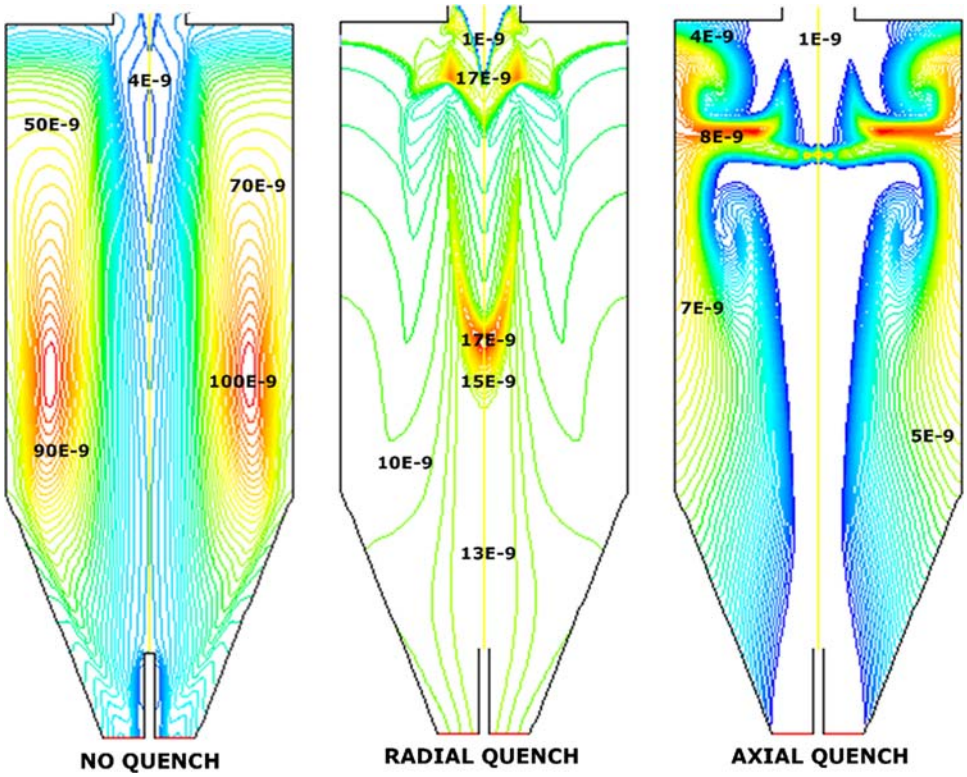


**Fig. 13** Numerical diameter (m) after nucleation + condensation

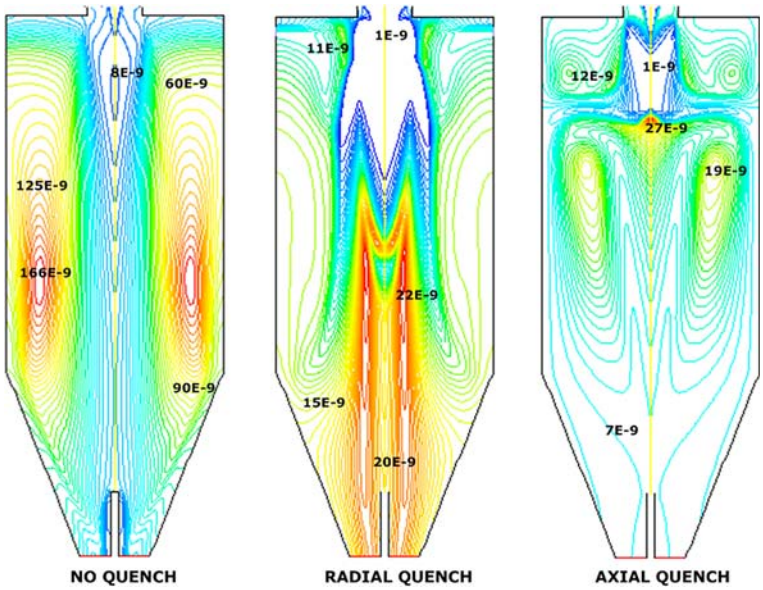


**Fig. 14** Numerical diameter (m) after nucleation + condensation + coagulation

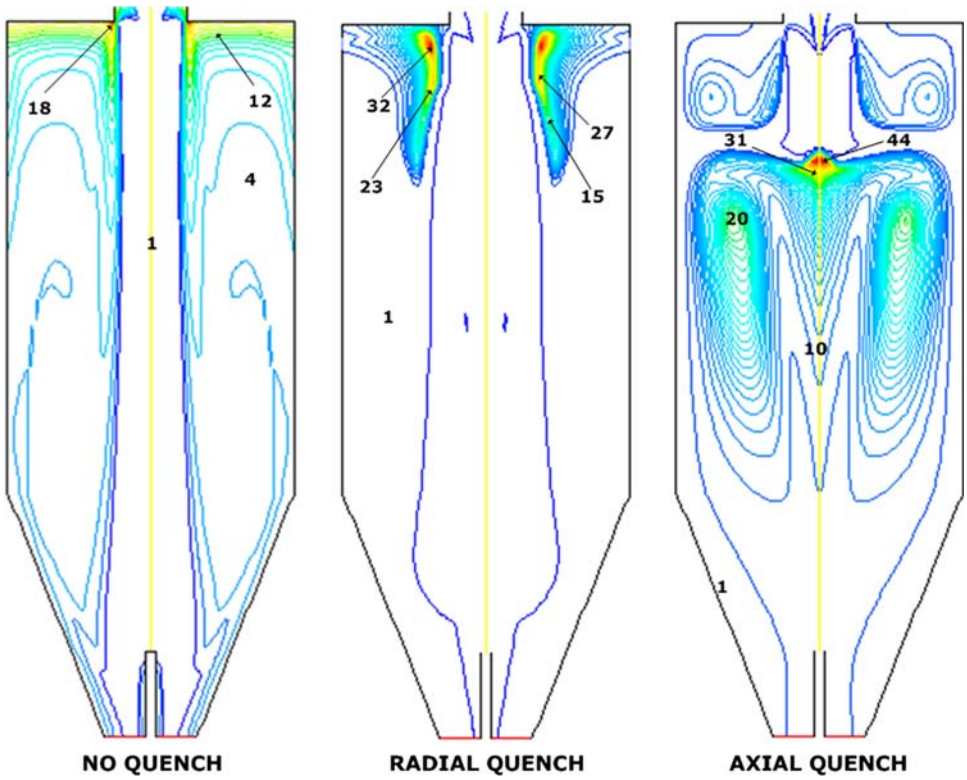


**Fig. 15** Average number of primary particles per aggregate

The results show that the quench strongly affects the temperature distribution inside the reactor. Consequently, the role of quench design is clearly shown to have a decisive impact on the final particle size and morphology. Moreover, it is observed that the particle injection rate has a cooling effect on plasma temperature, but in the range of precursor mass flow rates used in this study, this is not sufficient to reduce silica evaporation rates significantly. For the case without quench the level of turbulence is low but not negligible. The results show significant amount of silica vapor in the plasma zone, where the silica microparticles are evaporated. It is also observed that the

**Table 7 Summary of comparison between numerical and experimental results**

| Parameter | No quench | Axial quench | Radial quench | Wall tube |
|---|---|---|---|---|
| Diameter (Experimental) | 37 | 25 | 25 | 90 |
| Morphology (Experimental) | Spherical—partially aggregated | Large aggregated | Highly aggregated | Spherical |
| Diameter (Modeling) | 38 | 17 | 23 | 58 |
| Morphology (Modeling) | 20 | 44 | 32 | 4 |

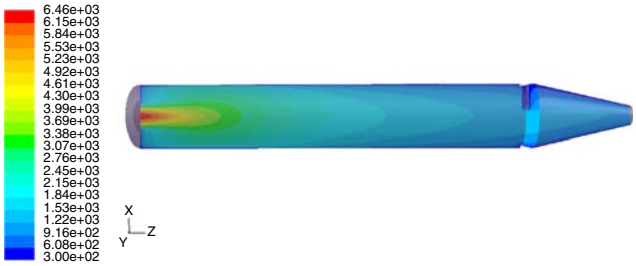


**Fig. 16** Wall tube temperature contours (K)

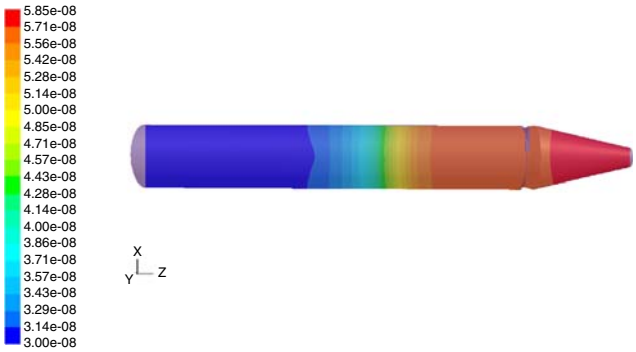


**Fig. 17** Wall tube numerical diameter contours (m)

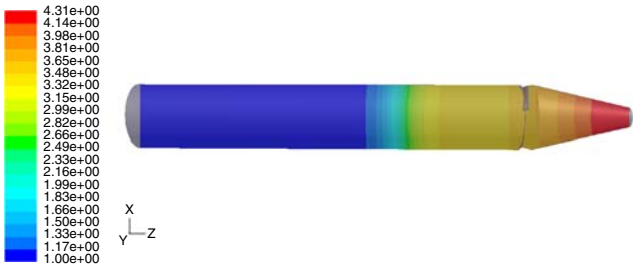


**Fig. 18** Wall tube number of primary particles per aggregate

nucleation mechanism is located early in the flame front and the post flame zone and the areas downstream the condensation reactor. The results obtained experimentally by Goortani et al. (Ref 9) are confirmed using the fractal aggregation model, namely, that it is possible to obtain spherical particles using an adequate quench and reactor configuration design. Growth mechanisms are governed by condensation and fractal coagulation processes. Formation of particles is directly affected by temperature and velocity recirculation. Near the wall, Brownian diffusion and thermophoresis are responsible for particle deposition. More fluid recirculation leads to more collisions between the particles and consequently more levels of aggregation among particles are observed (Ref 9). This suggests that the quench injection rate is one of the most important process parameters since it directly affects the location and final size of aggregates. Fractal particles are more present in the case of axial quench because of the increased number of possible interparticle collisions.

The present model is limited to particles in the free molecular regime and low raw material vapor concentrations; consequently, refinements in model predictions will lead to more accurate and precise predictions. The present particle aggregation model is developed assuming a constant aggregate fractal dimension $D_f$. A comparison of different values of $D_f$ could give a better approach to the fractal shape of particles. Since the quench strongly affects the particle size and morphology, a parametric study changing the flow rate of quench is suggested. The system silica-oxygen-argon is proposed as nonreactional system to simplify this study. A complete analysis of the reactional mechanism could improve the predictions of the present model.

The present work provides a qualitative and quantitative description of fractal growth of silica particles in thermal plasmas. Reported results are in good agreement with experimental findings of Goortani and co-workers (Ref 9, 22). This five-moment model used appears as a useful and practical method to assist scientists and engineers in the design of proper reactors to control the size and morphology of nanopowders produced using thermal plasma technology.

## References

1. F.E. Kruis, H. Fissan, and A. Peled, Synthesis of Nanoparticles in the Gas Phase for Electronic, Optical and Magnetic Applications—A Review, *J. Aerosol Sci.*, 1998, **29**(5-6), p 511-535
2. P.C. Kong and E. Pfender, Thermal Plasma Synthesis of Ceramics—A Review, *Heat Transfer Therm. Plasma Process. ASME*, 1991, **161**, p 1-8
3. G. Vissokov, I. Grancharov, and T. Tsvetanov, On the Plasma-Chemical Synthesis of Nanopowders, *Plasma Sci. Technol.*, 2003, **5**, p 2039-2050
4. N.Y. Mendoza-Gonzalez, B.M. Goortani, and P. Proulx, Numerical Simulation of Silica Nanoparticles Production in a RF Plasma Rector: Effect of Quench, *Mater. Sci. Eng. C*, 2007, **27**(5-8), p 1265-1269
5. N.Y. Mendoza-Gonzalez, B.M. Goortani, and P. Proulx, Numerical Study of the Synthesis of Nanoparticles in an Inductively Coupled Plasma Reactor, *Czech. J. Phys.*, 2006, **56-B**, p B1263-B1270

6. M. Shigeta, T. Watanabe, and H. Nishiyama, Numerical Investigation for Nanoparticle Synthesis in an RF Inductively Coupled Plasma, *Thin Solid Films*, 2004, **457**, p 192-200
7. R. Bolot, C. Coddet, C. Schreuders, M. Leparoux, and S. Siegmann, Modeling of an Inductively Coupled Plasma for the Synthesis of Nanoparticles, *J. Therm. Spray Technol.*, 2007, **16**(5-6), p 690-697
8. R. Ye, J.G. Lian, and T. Ishigaki, Controlled Synthesis of Alumina Nanoparticles Using Inductively Coupled Thermal Plasma with Enhanced Quenching., *Thin Solid Fims*, 2007, **515**(9), p 4251-4257
9. B.M. Goortani, P. Proulx, S. Xue, and N.Y. Mendoza-Gonzalez, Controlling Nanostructure in Thermal Plasma Processing: Moving from Highly Aggregated Porous Structure to Spherical Silica Nanoparticles, *Powder Technol.*, 2007, **175**, p 22-32
10. C.R. Kaplan and J.W. Gentry, Agglomeration of Chain-Like Combustion Aerosols due to Brownian Motion, *Aerosol Sci. Technol.*, 1988, **8**, p 11-28
11. A. Kazakov and M. Frenklach, Dynamic Modeling of Soot Particle Coagulation and Aggregation: Implementation with the Methods of Moments and Application to High-Pressure Laminar Premixed Flames, *Combust. Flame*, 1998, **114**, p 484-501
12. R.J. Samson, G.W. Mulholland, and J.W. Gentry, Structural Analysis of Soot Aggregates, *Langmuir*, 1987, **3**, p 272-281
13. T. Matsoukas and S.K. Friedlander, Dynamics of Aerosol Agglomerate Formation, *J. Colloid Interface Sci.*, 1991, **146**(2), p 495-506
14. M.K. Wu and S.K. Friedlander, Enhanced Power Law Agglomerate Growth in the Free Molecular Regime, *J. Aerosol Sci.*, 1993, **24**, p 273-282
15. Y. Xiong and S.E. Pratsinis, Formation of Agglomerate Particles by Coagulation and Sintering part I: A Two Dimensional Solution of the Population Balance Equation, *J. Aerosol Sci.*, 1993, **24**, p 283-300
16. F. Kruis, K. Kusters, and S. Pratsinis, Simple Model for the Evolution of the Characteristics of Aggregate Particles Undergoing Coagulation and Sintering, *Aerosol Sci. Technol.*, 1993, **19**, p 514-526
17. J. I. Jeong and M. Choi, A Sectional Method for the Analysis of Growth of Polydisperse Non-Spherical Particles Undergoing Coagulation and Coalescence, *J. Aerosol Sci.*, 2001, **32**, p 565-582
18. J.I. Jeong and M. Choi, Analysis of Non-Spherical Polydisperse Particle Growth in a Two-Dimensional Tubular Reactor, *J. Aerosol Sci.*, 2003, **34**, p 713-732
19. F. Aristizabal, R.J. Munz, and D. Berk, Modeling of the Production of Ultra Fine Aluminium Particles in Rapid Quenching Turbulent Flow, *Aerosol Sci. Technol.*, 2006, **37**, p 162–189
20. T. Adona, ''The Study of a Novel Thermal Process for the Production of Fumed Silica,'' PhD Thesis, McGill University, Canada, 1998
21. J.F. Bilodeau, ''Modélisation de la Croissance de Poudres Ultrafines en Réacteur à Plasma Thermique (Modeling of the Ultra Fine Particle Growth in a Thermal Plasma Reactor),'' PhD Thesis, Université de Sherbrooke, Canada, 1994, in French
22. B.M. Goortani, N.Y. Mendoza, and P. Proulx, Synthesis of $SiO_2$ Nanoparticles in RF Plasma Reactors: Effect of Feed Rate and Quench Gas Injection, *Int. J. Chem. Reactor Eng.*, 2006, **4:A33**, p 1-18
23. M.I. Boulos, Flow Temperature Fields in the Fire-Ball of an Inductively Coupled Plasma, *IEEE Trans. Plasma Sci.*, 1976, **4**, p 28-39
24. S. Xue, P. Proulx, and M.I. Boulos, Extended-Field Electromagnetic Model for Inductively Coupled Plasma, *J. Phys. D: Appl. Phys.*, 2001, **34**, p 1897-1906
25. R. Bolot, J. Li, and C. Coddet, Some Key Advices for the Modeling of Plasma Jets using Fluent, *Proceedings of the International Thermal Spray Conference*, ITSC 2005, 2-4 May 2005, (Basel, Switzerland), DVS Verlag GmbH, Düsseldorf, Germany, CD-Room, ISBN: 3-87155-793-5
26. R. Ye, P. Proulx, and M.I. Boulos, Particle Turbulent Dispersion and Loading Effects in an Inductively Coupled Radio Frequency Plasma, *J. Phys. D: Appl. Phys.*, 2000, **33**(17), p 2154-2162
27. M. Shigeta and H. Nishiyama, Numerical Analysis of Metallic Nanoparticle Synthesis Using RF Inductively Coupled Plasma Flows, *Trans. ASME*, 2005, **127**, p 1222-1230
28. P. Proulx, J. Mostaghimi, and M.I. Boulos, Heating of Powers in an RF Inductively Coupled Plasma Under Dense Loading Conditions, *Plasma Chem. Plasma Process.*, 1987, **7**(1), p 29-53
29. M.I. Boulos and W.H. Gauvin, The Plasma Jet as a Chemical Reactor, a Proposed Model, *Can. J. Chem. Eng.*, 1974, **52**(3), p 355-363
30. L. Talbot, R.K. Chen, R.W. Schefer, and D.R. Willis, Thermophoresis of Particles in a Heated Boundary Layer, *J. Fluid Mech.*, 1980, **101**(4), p 737-758
31. H. Ounis, G. Ahmadi, and J.B. McLaughlin, Brownian Diffusion of Submicrometer Particles in the Viscous Sublayer, *J. Colloid Interface Sci.*, 1991, **143**(1), p 266-277
32. A. Li and G. Ahmadi, Dispersion and Deposition of Spherical Particles from Point Sources in a Turbulent Channel Flow, *Aerosol Sci. Technol.*, 1992, **16**(4), p 209-226
33. W.E. Ranz and W.R. Marshall, Evaporation from Drops, Part I, *Chem. Eng. Prog.*, 1952, **48**(3), p 141-146
34. W.E Ranz and W.R Marshall, Evaporation from Drops, Part II, *Chem. Eng. Prog.*, 1952, **48**(4), p 173-180
35. S.L. Girshick and C.P. Chiu, Kinetic Nucleation Theory: A New Expression for the Rate of Homogeneous Nucleation from an Ideal Supersaturated Vapor, *J. Chem. Phys.*, 1990, **93**, p 1273-1277
36. J.H. Seinfeld, Atmospheric Chemistry and Physics of Air Pollution. John Wiley & Sons, New York, 1986
37. G.M. Phanse and S.E. Pratsinis, Theory for Aerosol Generation in Laminar Flow Condensers, *Aerosol Sci. Technol.*, 1989, **11**(2), p 100-119
38. S. Vemury and S. Pratsinis, Self-Preserving Size Distributions of Agglomerates, *J. Aerosol Sci.*, 1995, **26**, p 175-185
39. G.W. Mulholland, R.J Samson, R.D. Mountain, and M.H. Ernst, Cluster Size Distribution for Free Molecular Agglomeration, *Energy Fuels*, 1988, **2**, p 481-486
40. D. Lindackers, M. Strecker, P. Roth, C. Janzen, and S.E. Pratsinis, Formation and Growth of $SiO_2$ Particles in Low Pressure $H_2/O_2$/Ar Flames Doped with $SiH_4$, *Combust. Sci. Technol.*, 1997, **123**, p 287-315
41. E. Pantos, J.B. West, W.H. Dokter, H.F. Van Garderen, and R.A. Van Santen, Growth and Aging Phenomena in Silica Gels, *J. Sol-Gel Sci. Technol.*, 1994, **2**, p 273-276
42. C.G. Wells, N.M. Morgan, M. Kraft, and W. Wagner, A New Method for Calculating the Diameter of Partially-Sintered Nanoparticles and its Effect on Simulated Particle Properties, *Chem. Eng. Sci.*, 2006, **64**(1), p 158-166
43. M. Frenklach and S.J. Harris, Aerosol Dynamics Modeling Using the Method of Moments, *J. Colloid Interface Sci.*, 1987, **118**, p 252-261
44. M.I. Boulos, P. Fauchais, and E. Pfender, *Thermal Plasmas: Fundamentals and Applications*, Plenum Press, New York, 1994
45. P. Proulx, J. Mostaghimi, and M.I. Boulos, Plasma-Particle Interaction Effects in Induction Plasma Modeling Under Dense Loading Conditions, *Int. J. Heat Mass Transfer*, 1985, **28**, p 1327-1336
46. M. Shigeta and T. Watanabe, Numerical Investigation of Cooling Effect on Platinum Nanoparticle Formation in Inductively Coupled Thermal Plasmas, *J. Appl. Phys.*, 2008, **103**, p 074903
47. J.F. Bilodeau and P. Proulx, A Mathematical Model for Ultrafine Iron Powder Growth in a Thermal Plasma, *Aerosol Sci. Technol.*, 1996, **24**, p 175-189
48. M. Shigeta and T. Watanabe, Two Dimensional Analysis of Nanoparticle Formation in Induction Thermal Plasmas with Counterflow Cooling, *Thin Solid Films*, 2008, **103**, p 4415-4422